Importance of Interfacial Band Structure between the Substrate and Mn₃O₄ Nanocatalysts during Electrochemical Water Oxidation

Moo Young Lee,[†,§] Heonjin Ha,[†,§] Kang Hee Cho,[†] Hongmin Seo,[†] Sunghak Park,[†] Yoon Ho Lee,[†] Sung-Joo Kwon,[‡] Tae-Woo Lee,[†] and Ki Tae Nam[*,†]

[†]Department of Materials Science and Engineering, Seoul National University, Seoul 08826, Republic of Korea

[‡]Department of Materials Science and Engineering, Pohang University of Science and Technology (POSTECH), Pohang, Gyungbuk 37673, Republic of Korea

S Supporting Information

ABSTRACT: The charge transport in the film-type electrocatalysts for the oxygen evolution reaction is a significant factor affecting the overall catalytic performance. For instance, transition metal oxide-based catalysts film has an optimum coating thickness due to the charge transport limitation. In this article, we investigated the charge transport behavior at the interface between the catalysts and the underlying substrate, which has been less investigated than the two other charge-transporting interfaces, that is, the catalysts surfaces and the inner catalysts film. We observed that Mn₃O₄ nanocatalysts exhibited different oxygen-evolving performances depending on the underlying substrate, and this activity trend was correlated with the work function of the substrate. We analyzed the work function dependency based on the energy band structure at the catalysts−substrate interface and determined that the substrates with low work functions formed high Schottky barriers, disturbing the interfacial charge transport. On the basis of this understanding, we demonstrated that the catalytic activity of Mn₃O₄ nanocatalysts film can be significantly enhanced using industrially important Ti substrates that have a thin buffering interlayer with the proper work function.

KEYWORDS: electrocatalysis, water oxidation, oxygen evolution reaction, substrate effect, band structure, Mn₃O₄ nanoparticles
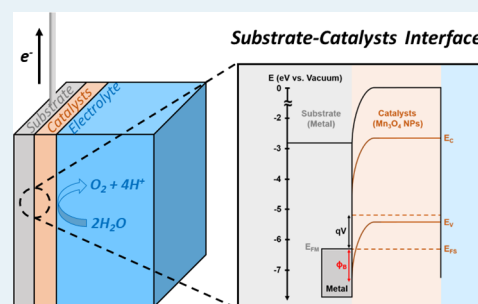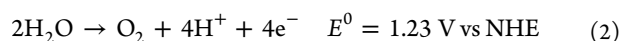
1. INTRODUCTION

The increased energy demand due to global population growth has given rise to the increased use of fossil fuels, highlighting the importance of sustainable and clean energy sources.[1] Among the suggested alternative energy sources, hydrogen has been regarded as a promising one because of its high energy density and abundant raw materials, which can also be produced through sustainable energy conversion processes. In particular, water electrolysis is one of the most appropriate pathways for sustainable hydrogen production without generating any byproducts, which is in contrast with conventional carbon-based methods.[2]

Water electrolysis consists of two half-reactions: the hydrogen evolution reaction (HER, eq 1) and the oxygen evolution reaction (OER, eq 2). To implement a water electrolysis system for practical applications, it is essential to develop robust electrocatalysts for lowering the activation barrier of each half-reaction. Numerous strategies for designing HER/OER catalysts have been extensively suggested, followed by the development of remarkable HER/OER catalysts exhibiting low overpotentials; however, limitations on the realization of a practical water electrolysis system remain due to the critical drawback at the anodic compartment, that is, the inherently slow reaction kinetics of OER.[3] Kinetically, four proton-coupled electron transfers are required to complete the

oxygen-evolving catalytic cycle; thus, OER presents more complicated reaction steps than does HER, where only two electrons are involved. In addition, the O−O bonding formation for releasing dioxygen molecules has a high activation barrier; thus, a high overpotential is inevitably required to accomplish OER.[4−6]

$$2H^+ + 2e^- \rightarrow H_2 \quad E^0 = 0 \text{ V vs NHE} \tag{1}$$

$$2H_2O \rightarrow O_2 + 4H^+ + 4e^- \quad E^0 = 1.23 \text{ V vs NHE} \tag{2}$$

Generally, precious metal oxides, such as RuO₂ and IrO₂, are known to exhibit the best catalytic performance for OER; however, because of their expensiveness and scarcity, attempts to reduce their contents[7−10] and replace them with earth-abundant elements should be required. Indeed, 3d transition metal oxides have been intensively explored as proper candidates for replacing current precious metal oxides.[11,12] For example, Ni and Fe hydroxides exhibit great catalytic activities under basic conditions, exhibiting low overpotentials (~200 mV at 10 mA/cm²) superior to that of IrO₂.[13−15] Under the neutral condition, electrodeposited amorphous

cobalt oxides (Co-Pi) manifest a great catalytic performance with almost permanent stabilities through self-healing processes.[16]

In nature, the water oxidizing complex (WOC) in the biological photosystem II exhibits a great OER activity with a high turnover frequency ($\sim$50 O_2 molecules s^{-1}), superior to any artificial OER catalysts.[17] The Mn_4CaO_5 cluster known as the catalytic site in WOC has an asymmetric and distorted structure that allows for flexible valency changes of Mn atoms as well as dynamic structural changes of the cluster during water oxidation.[18−21] Inspired by the unique features of the Mn_4CaO_5 cluster, bioinspired Mn-based catalysts have been intensively investigated. Generally, bulk Mn oxides such as MnO or Mn_2O_3 exhibit a poor OER performance due to their limited redox capabilities at each phase.[22] On the basis of this understanding, mixed-valent MnO_x catalysts have been developed that enable flexible changes to the Mn oxidation state. The Driess group synthesized MnO_x nanoparticles (NPs) via a surface treatment by using Ce(IV) oxidants, and electrodeposited amorphous and disordered MnO_x films were developed by the Dau group.[23,24] Both MnO_x catalysts showed a high OER performance at neutral pH, which could be attributed to the inherent mixed Mn valency. In addition, the Dismukes group observed that the OER performance of Mn oxides was enhanced as the Mn(III)−O bond was elongated by a Jahn−Teller (J−T) distortion, and the Nakamura group showed that the stabilization of Mn(III) in J−T distorted MnO_2 NPs could prevent charge disproportionation and, thus, enhance the OER performance.[25,26]

Our group previously developed $Mn_3(PO_4)_2 \cdot 3H_2O$ nano-catalysts in which the phosphate ions distorted the crystal structures and stabilized Mn(III), exhibiting a better OER performance than that of pure crystalline Mn oxides at neutral pH.[27] Furthermore, we successfully synthesized uniform and assembled partially oxidized MnO NPs with a superior OER performance to that of conventional bulk Mn-based catalysts. Distinct from the bulk Mn oxides, we confirmed that the Mn(III) species were highly stabilized on the surface of MnO NPs. Through comprehensive electrokinetic and in situ spectroscopic analyses, we suggested a unique reaction mechanism whereby the rate-determining step (RDS) was the O−O bonding formation step, which was highly different from the bulk Mn oxide cases.[28,29] Recently, we further investigated the electron transport behaviors of our MnO NPs during OER by using electrochemical impedance spectroscopy (EIS) analysis and successfully extracted various kinetic parameters for surface catalysis.[30]

On the basis of our mechanistic understanding of the film-type OER catalysts, we believe that controlling the charge transport behaviors of the catalyst film is as important as improving the intrinsic activity of the catalysts, which has also been pointed out by several groups.[31−33] In this regard, to establish a rational design rule for film-type electrocatalysts, the charge-transporting characteristics of every single process should be investigated for simplifying the whole process and decoupling the affecting variables. We think that the overall charge transport in the film-type electrocatalysts can be divided into three interfacial processes: the electrons for water oxidation should transport through (i) the electrolyte−catalysts interface, (ii) the inner catalysts film, and (iii) the catalysts−substrate interface.

In the charge transfer process at the electrolyte−catalysts interface, the intrinsic properties of the catalytic materials determine the surface capacitance and resistance, which are usually analyzed and quantified by EIS. To extract the proper charge transfer parameters by EIS analysis, the design of an appropriate equivalent circuit of the hydrous layer, where the electrolyte and catalysts coexist, is required. Indeed, there have been abundant investigations on modeling elaborated equivalent circuits that closely correspond to the experimental EIS data, giving insight into understanding the interfacial charge transfer between the electrolyte and catalysts.[30,32,34]

In the charge transport process throughout the inner catalysts film, the loading amount of the catalysts film is an important factor. The analogous loading-dependent activity trends have previously been studied for transition metal (oxy)hydroxides such as NiO_x, FeO_x, and MnO_x.[32] Generally, under low loading conditions, an OER activity enhancement was observed that could be explained by the increase in the surface area with the film thickness. At higher loadings, the optimized OER activity was obtained in the region and the surface area remained constant regardless of the thickness increase. At even higher loadings, a decrease in the OER activity was observed, which was attributed to the significant electron transport resistance across the catalysts film. In the case of Co-Pi, a well-known film-type catalyst, it has been reported that the exchange current density saturated at a 3 μm thickness, and we have also observed that our MnO NPs film exhibited optimum catalytic activity at a 300 nm thickness.[29−31,33]

In the charge transport at the catalysts−substrate interface, the adhesion of the catalysts to the substrate and the electronegativity of the substrate have been suggested as affecting factors.[35] It has been reported that strong physical adhesion between catalysts and substrates lowered the film resistance and enhanced the overall OER performance for the film-type catalysts.[36] In addition, the Bell group suggested that metal substrates with a high electronegativity strongly attracted the electrons of Co_3O_4, which facilitated the charge transport at the catalysts−substrate interface as well as the valency change of the Co atoms.[37]

Among the three charge transport processes in film-type electrocatalysts, the charge transport at the catalysts−substrate interface has been less considered than the others, where studies have solely focused on the physical adhesions of the catalysts and not on the electrical properties of the substrate. This discrepancy is due to (i) the assumption that the water oxidation reaction would be substantially more sluggish than the charge transport and (ii) the previous experimental experiences with highly conductive metallic catalysts such as Pt, RuO_2, and IrO_2.[38,39] However, in the case of earth-abundant element-based oxides or compounds, the interfacial resistance is high and significantly depends on the substrate. In the case of our Mn_3O_4 nanoparticles, the OER activity was very high when deposited on a fluorine-doped tin oxide-coated glass (FTO) substrate, and the potential required to reach 1 mA/cm^2 was 1.23 V vs NHE in neutral 0.5 M phosphate buffer solution. However, when deposited on a Ti substrate, which is widely used in commercial electrolysis and is industrially relevant, the potential required to reach 1 mA/cm^2 significantly increased to 1.57 V vs NHE under the same conditions. These observations are a puzzling phenomenon, which was not expected for Pt, IrO_2, and RuO_2 catalysts; thus, we attempt to understand the reason for the decrease in OER activities caused by the underlying Ti substrate.

In this study, we aim to investigate how the underlying substrate can affect the overall electrochemical properties of film-type electrocatalysts for OER. We systematically measured the substrate-dependent OER activity of Mn_3O_4 NPs and analyzed the electron transport behaviors to understand the different catalytic activities of Mn_3O_4 NPs depending on the underlying substrates by conducting EIS analysis and modeling the interfacial band structure. We found that the electronic energy band structure at the catalysts−substrate interface clearly affected the overall OER performance, which could be controlled by tuning the interfacial band structure.

2. EXPERIMENTAL SECTION

2.1. Materials. Manganese(II) acetate tetrahydrate (Mn-$(CH_3COO)_2\cdot4H_2O$, 99%, Acros), oleylamine ($C_{18}H_{35}NH_2$, 70%, Sigma-Aldrich), oleic acid ($CH_3(CH_2)_7CH=CH-(CH_2)_7COOH$, 99%, Alfa Aesar), and 1-octanol ($CH_3(CH_2)_7OH$, 99%, Alfa Aesar) were purchased and used as received without further purification. Nickel foil (0.1 mm thick, 99.5%, Alfa Aesar), stainless steel (SS) foil (0.1 mm thick, type 304, Alfa Aesar), copper foil (0.127 mm thick, annealed, 99.9%, Alfa Aesar), titanium foil (0.127 mm thick, annealed, 99%, Alfa Aesar), zirconium foil (0.25 mm thick, annealed, 99.8%, Alfa Aesar), and FTO (NSG TEC A8, Pilkington) with a surface resistivity of 7 Ω/sq were purchased and used.

2.2. Synthesis of the 4 nm-sized Mn_3O_4 NPs. The 4 nm-sized Mn_3O_4 NPs were synthesized through a modification of the previously reported thermal decomposition method.[40,41] A mixture of manganese(II) acetate tetrahydrate (0.49 g), oleic acid (1.139 g), and oleylamine (6.054 g) dissolved in 1-octanol (30 mL) was stirred at room temperature for 3 h in a 100 mL flask. Then, the mixture was heated to 100 °C under magnetic stirring at 1500 rpm. When the temperature reached 99 °C, deionized water (0.38 mL) at room temperature was injected rapidly into the mixture and the temperature was maintained at 100 °C for 10 min. Finally, the dark brown solution was then cooled to room temperature.

2.3. Electrode Preparation. All the substrates were sonicated for 30 s with acetone, ethanol, and deionized water. After sonication, the metal foils were further cleaned by immersing in a 0.5 M H_2SO_4 solution at 60 °C for 1 h. The metal interlayer was deposited on FTO and Ti substrates by radiofrequency sputter (MHS-1500, Moohan, Korea) at 300 W. The Mn_3O_4 NPs crude solution, toluene, and acetone were mixed in a volume ratio of 1:1:2 and centrifuged to obtain the precipitate of the Mn_3O_4 NPs. The purification step was repeated several times by reinserting the equivalent amounts of toluene and acetone. After this purification step, the precipitated NPs were dispersed in *n*-hexane. Then, 40 μL of the Mn_3O_4 NPs solution was spin-coated onto the substrates at a spin rate of 2000 rpm and a holding time of 15 s. The thickness of the Mn_3O_4 NPs film spin-coated on the substrates was controlled by the volume ratio of the initial dark brown Mn_3O_4 NPs solution to *n*-hexane. To eliminate the surfactants on the surface of the Mn_3O_4 NPs, which could inhibit the access of water molecules to active sites, the spin-coated films were annealed at 200 °C for 1 h.

2.4. Characterization of 4 nm-sized Mn_3O_4 NPs.
2.4.1. Transmission Electron Microscopy. Transmission electron microscopy (TEM) images were obtained using a high-resolution transmission electron microscope (LIBRA 120, Carl Zeiss, Germany) with an acceleration voltage of 120 kV.

To prepare the TEM samples, the Mn_3O_4 NPs dispersed in hexane were dropped on the TEM grid and dried in air.

2.4.2. Scanning Electron Microscopy. The morphology and thickness of the Mn_3O_4 NPs film on the various substrates were characterized by a focused ion beam (FIB) scanning electron microscope (AURIGA, Carl Zeiss, Germany). The images were taken with an acceleration voltage of 30 kV.

2.4.3. X-ray Photoelectron Spectroscopy. The X-ray photoelectron spectroscopy (XPS) analysis was conducted using an X-ray photoelectron spectrometer (K-alpha+, ThermoFisher Scientific, U.S.A.) with a pass energy of 40 eV and a step size of 0.1 eV. The XPS spectra of the Mn_3O_4 NPs were calibrated with C 1s peak (284.8 eV) as the standard reference.

2.4.4. Ultraviolet Photoelectron Spectroscopy. The ultraviolet photoelectron spectroscopy (UPS) analysis of the Mn_3O_4 NPs film was carried out by a photoelectron spectrometer (PHI 5000 VersaProbe, ULVAC PHI, Japan) using He I excitation (21.22 eV) with a pass energy of 0.585 eV and a sample bias of −9 eV. The resulting spectrum was plotted against the binding energy for the calculation of the valence band position of the Mn_3O_4 NPs. The binding energy of the Mn_3O_4 NPs was calculated from the following equation,

$$h\nu = E_B + E_K + \Phi_{analyzer}$$

where $h\nu$ is the light energy of He I, and E_B, E_K, and $\Phi_{analyzer}$ are the binding energy measured from the Fermi level, the kinetic energy, and the work function of the analyzer, respectively.[42]

2.4.5. Ultraviolet−Visible Spectroscopy. The UV−vis absorption spectrum was obtained in absorbance mode using a UV−vis spectrophotometer (UV-2550, Shimadzu, Japan) in a wavelength range from 300 to 900 nm.

2.4.6. Kelvin Probe Force Microscopy. The work function values of the substrates were measured using a scanning Kelvin probe (SKP5050, Kelvin Probe Technology, Scotland), which is a device that measures the surface electrical potential without actually contacting the sample.[43] The work function of the surface was calculated from the potential difference between the surface and the Au tip, for which the work function value is already known.

2.5. Electrochemical Measurements. All electrochemical measurements were conducted in a three-electrode system. Ag/AgCl/3 M NaCl and Pt were used as the reference electrode and counter electrode, respectively. The electrode potential vs Ag/AgCl was converted to the normal hydrogen electrode (NHE) scale, using the following equation: E(NHE) = E(Ag/AgCl) + 0.210 V. Additionally, the overpotential values were calculated by the difference between the *iR*-corrected potential ($V = V_{applied} − iR$) and the thermodynamic potential of water oxidation at a specified pH. The 0.5 M phosphate buffer solution (pH 7) was used as the electrolyte. We did not observe any Pt contents on the anode electrode after the electrochemical experiments by measuring XPS spectrum, indicating that the Pt counter electrode did not affect the catalytic activity at the working electrode (Figure S1).

2.5.1. Cyclic Voltammetry. Cyclic voltammetry (CV) experiments were carried out at room temperature using a potentiostat (VSP-300, Bio-Logic Science Instruments, France). Prior to every cyclic voltammetry measurement, the solution resistance was measured and all the data were *iR*-compensated. The CV curves were polarization-corrected to

remove the nonfaradaic contribution. The scan rate for all CV curves was 50 mV/s. During the analysis, the electrolyte was stirred by a magnetic bar to remove the oxygen bubbles on the surfaces of the electrodes.

2.5.2. Electrochemical Impedance Spectroscopy. The electrochemical impedance spectroscopy (EIS) analysis was performed at room temperature using a potentiostat (CHI 760E, CH Instruments, U.S.A.). The experiment was conducted in the frequency range from 10^{-1} to 10^{5} Hz with a 5 mV amplitude. The fitting was performed with the commonly used complex nonlinear least-squares (CNLS) fitting technique in the software (ZView 2, Scribner Associates, U.S.A.).

3. RESULTS AND DISCUSSION

The 4 nm-sized Mn_3O_4 NPs were synthesized by the thermal decomposition method modified from previous reports,[40,41] and Figure 1a clearly shows the uniform morphology of the 4 nm-sized NPs. The electrodes were prepared by spin-coating onto FTO glass and Ni, stainless steel (SS), Cu, Ti, and Zr foils, and the coating thickness of the Mn_3O_4 NPs was

Figure 1. (a) TEM image of the synthesized Mn_3O_4 nanoparticles (NPs) approximately 4 nm in size. (b) Cross-sectional SEM images of Mn_3O_4 NPs spin-coated on fluorine-doped tin oxide-coated glass (FTO) and Ti foil. (c) Samples coated with Mn_3O_4 NPs on FTO, Ni, stainless steel (SS), Cu, Ti, and Zr substrates.

controlled as 150 nm regardless of the underlying substrate (Figure 1b), to exclude the possible effect on the OER activity due to the amount of the catalysts. All the electrodes used in this study are displayed in Figure 1c.

We first measured the substrate-dependent OER performance of the Mn_3O_4 NPs. The polarization-corrected cyclic voltammetry curves of Mn_3O_4 NPs in the neutral 0.5 M phosphate buffer solution were clearly dependent on the underlying substrate (Figure 2a). The overpotentials of Mn_3O_4 NPs required to reach a current density of 1 mA/cm² were measured as 411, 418, 426, 592, and 740 mV on FTO, Ni, SS, Cu, and Ti substrates, respectively. In the case of Mn_3O_4 NPs on the Zr substrate, the current density did not reach 1 mA/cm² within the potential sweep window (from open-circuit potential to 1.4 V vs Ag/AgCl) of our CV measurement. Compared with previously reported transition metal-based electrocatalysts for OER at neutral pH, summarized in Table S1, Mn_3O_4 NPs/FTO exhibited the highly efficient OER activity under neutral condition, which became poor on the other substrates. We also measured the substrate-dependent stability of the Mn_3O_4 NPs by chronopotentiometry at 10 mA/cm² (Figure S2). The results show a similar trend of substrate dependency of the OER activity of Mn_3O_4 NPs. Because we controlled the thicknesses of the Mn_3O_4 NPs films to be identical, the substrate-dependent difference in the OER performance was evidently caused by the substrate materials. In other words, the charge transport behavior at the Mn_3O_4 NPs−substrate interface was the main cause of the change in the OER performance of Mn_3O_4 NPs because the nature of the charge transports at the electrolyte−Mn_3O_4 NPs interface and in the inner Mn_3O_4 NPs film remained the same under our experimental conditions.

In addition, the amounts of dissolved Mn_3O_4 NPs on FTO and Ti substrates during the electrolysis at 1 mA/cm² for 12 h were similarly measured by inductively coupled plasma mass spectrometry (ICP-MS), resulting in 1.45 and 1.10 μg, respectively. This result excluded the possibility of different dissolution behaviors depending on the underlying substrate. Therefore, we assumed that the poor performances provided in the Cu, Ti, and Zr cases in Figure 2a originated from the sluggish charge transport at the Mn_3O_4 NPs−substrate interface, distinct from the FTO, Ni, and SS cases.

To quantify the charge transport at the Mn_3O_4 NPs−substrate interface, EIS analysis under the OER condition was carried out (Figure 2c and d). We obtained the Nyquist plots for the four electrodes at applied anodic potentials of 1.30 and 1.35 V (vs NHE), as displayed in parts c and d of Figure 2, respectively. The equivalent circuit model we adopted is presented in the inset of Figure 2d, and it has been a widely accepted circuit model for film-type transition metal oxide catalysts.[34] Through fitting our experimental data with this circuit model, several charge transport parameters were extracted and are summarized in Table S2. We chose Mn_3O_4 NPs/FTO and Mn_3O_4 NPs/Ti as representative electrodes exhibiting good and poor OER activities, respectively. We also prepared two other Au film-inserted electrodes (Mn_3O_4 NPs/Au/FTO and Mn_3O_4 NPs/Au/Ti) to investigate the effect of the interlayer between Mn_3O_4 NPs and the substrate, which will be discussed later.

Taking a look at the total charge transfer resistance for the overall OER process (R1) of Mn_3O_4 NPs/FTO and Mn_3O_4 NPs/Ti, the R1 values of both electrodes decreased as the applied anodic potential increased, indicating that the whole
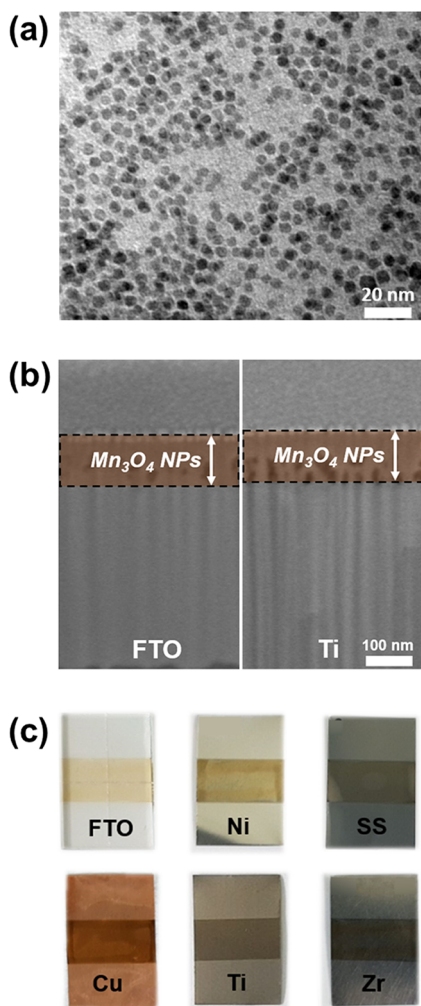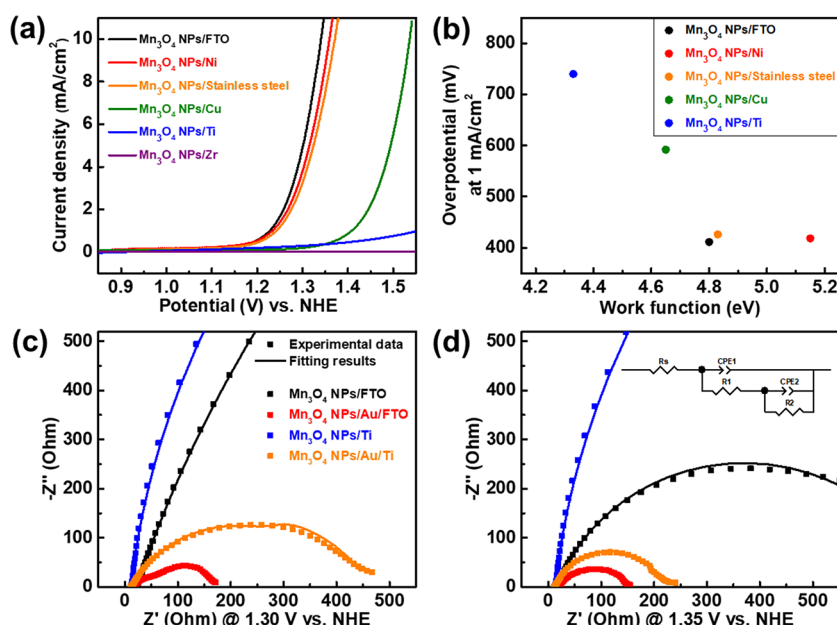
Figure 2. (a) Polarization-corrected cyclic voltammetry curves of Mn_3O_4 nanoparticles (NPs) on different substrates in 0.5 M phosphate buffer solution at pH 7 (scan rate: 50 mV/s). (b) Plot of the overpotential required to reach 1 mA/cm^2 vs the work function of the substrate. Experimental electrochemical impedance spectroscopy (EIS) data and fitting results for Mn_3O_4 NPs on the various substrates at (c) 1.30 V and (d) 1.35 V vs NHE in 0.5 M phosphate buffer solution at pH 7; the equivalent circuit used in the CNLS fitting (inset).
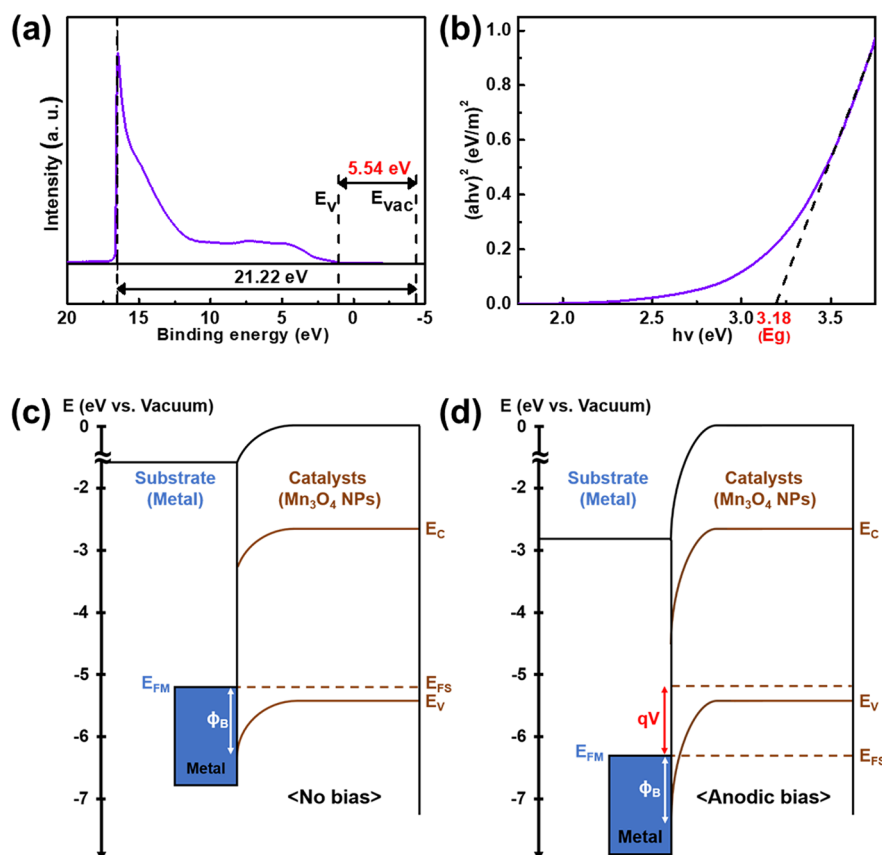

Figure 3. (a) Ultraviolet photoelectron spectroscopy (UPS) spectrum of Mn_3O_4 nanoparticles (NPs). (b) Tauc plot of Mn_3O_4 NPs from the UV−vis absorption spectrum. Schematic band structure of Mn_3O_4 NPs−substrate interface with (c) no bias and (d) anodic bias.

charge transport process from the catalytic surface to the electrode increased with the driving anodic potential. However, by comparing the R1 values of the two electrodes, the R1 of Mn_3O_4 NPs/Ti was measured as 5−8 times that of Mn_3O_4 NPs/FTO. As discussed in Figure 2a, the two electrodes possessed the same thickness Mn_3O_4 NPs films; thus, the different R1 values were apparently caused by the different interfaces between the Mn_3O_4 NPs and substrates. Therefore,

we could suggest that the charge transport at the Mn_3O_4 NPs/Ti substrate interface was inefficient compared to that at the Mn_3O_4 NPs/FTO substrate.

We further investigated the key factors affecting the rate of the charge transport at the catalysts−substrate interface and found that the work function of the substrate was closely correlated with the OER performance. Figure 2b shows the correlation between the overpotential required to reach a current density of 1 mA/cm^2 and the work function of the substrate. In the case of SS, the work function varies depending on the ratio of the Ni, Fe, and Cr elements; thus, we measured the work function of SS (4.83 eV) by Kelvin probe force microscopy (KPFM), which is a general tool for work function measurements. The work functions of the other substrates (except SS) were obtained from the well-known values of 4.80 (FTO), 5.15 (Ni), 4.65 (Cu), 4.33 (Ti), and 4.05 eV (Zr).[44] We observed two apparent phenomena in Figure 2b: (i) the OER performance became poor with the increase in overpotential as the work function decreased, and (ii) the OER performance saturated at similar overpotentials (∼420 mV at 1 mA/cm^2) when the work function was >4.80 eV. We suggested that those phenomena could be interpreted by the energy barriers between Mn_3O_4 NPs and the substrates based on the interfacial band structure model.

Generally, Mn_3O_4 is known as a typical p-type semiconductor; therefore, we assumed that the Fermi level of Mn_3O_4 NPs was close to the valence band level, which was measured by ultraviolet photoelectron spectroscopy (UPS) (Figure 3a). As shown in Figure 3a, the valence band position (E_V) of the Mn_3O_4 NPs was calculated from the difference between the vacuum level (E_{vac}) and the onset point in the low-binding-energy region (0.87 eV). E_{vac} was determined by subtracting the He I source energy (21.22 eV) from the secondary electron cutoff energy in the high-binding-energy region (16.55 eV), resulting in −4.67 eV. Therefore, the E_V of Mn_3O_4 NPs was calculated to be −5.54 eV vs E_{vac}. In addition to the measurement of the valence band position, UV−vis spectroscopy was conducted to determine the conduction band position (E_C) of Mn_3O_4 NPs from the bandgap energy (E_g) measurement (Figure 3b). The E_g of Mn_3O_4 NPs could be measured from the following equation,

$$\alpha(h\nu) = A(h\nu - E_g)^{1/n}$$

($n = 1$ for direct allowed transitions such as Mn_3O_4)

where α, $h\nu$, and A are the absorption coefficient, the light energy, and a constant, respectively. Therefore, the E_g of Mn_3O_4 NPs was identical to the intersection energy value between the extension line of the constant-slope region and the x-axis ($h\nu = 0$) in the Tauc plot of Mn_3O_4 NPs (Figure 3b), resulting in 3.18 eV. From E_V and E_g measured by UPS and UV−vis spectroscopy, respectively, the E_C of Mn_3O_4 NPs was calculated to be −2.36 eV vs E_{vac}.

On the basis of the energy band positions of Mn_3O_4 NPs, we modeled the interfacial band structure of the Mn_3O_4 NPs−substrate interface. Figure 3c depicts the interfacial band structure without any bias. Considering the work function of the substrates (<5.15 eV) and the Fermi level of Mn_3O_4 NPs (close to −5.54 eV), a typical metal−semiconductor (p-type) Schottky contact is formed. In detail, as the substrate and Mn_3O_4 NPs are contacted and as equilibrium is established, the electrons move from the anode to the cathode through the conducting wire, allowing downward movement of the Fermi

energy of the substrate (E_{FM}) and the corresponding downward bend of the Mn_3O_4 NPs energy band near the contact. As a result, a Schottky barrier is formed at the interfacial contact, for which the height (Φ_B) is determined to depend on the work function of the substrate. Generally, Schottky barriers hinder the interfacial transport of the majority carriers; however, some amount of the majority carriers can transport through the interface due to thermal excitation. Following the Boltzmann distribution, the number of transported carriers exponentially increases as Φ_B decreases, indicating that the work function of the substrate affects the rate of the interfacial charge transport. Figure 3d shows the interfacial band structure of the Mn_3O_4 NPs−substrate interface at an applied anodic bias. As an anodic potential (V) is applied, E_{FM} and the Fermi level of Mn_3O_4 NPs (E_{FS}) move down together by qV, with the charge of q. Therefore, Φ_B does not change before or after applying the anodic bias and solely depends on the work function of the substrate.

Taken together, we suggested that the substrate-dependent OER performance of Mn_3O_4 NPs could be analyzed using this aspect of our interfacial band structure model. First, the height of Schottky barrier was solely dependent on the work function of the substrate in our substrate effect measurements because the valence band position of Mn_3O_4 NPs was constant. Therefore, the number of the transported carriers at the Mn_3O_4 NPs−substrate interface decreased exponentially as the work function of the substrate decreased, resulting in the sluggish OER kinetics and poor catalytic performance observed in Figure 2b. Second, as the work function of the substrate exceeded a certain value (4.80 eV in our cases), sufficient charge carriers could be injected from the Mn_3O_4 NPs film into the substrate with sufficiently fast kinetics. The overall OER performance was then determined by the intrinsic OER activity of Mn_3O_4 NPs, implying that the whole charge transport process at the anode was not dominantly affected by the interfacial energy barrier. Therefore, the catalytic performances of Mn_3O_4 NPs using FTO, Ni, and SS substrates were similar, as shown in Figure 2a. On the basis of our understanding of the interfacial band structure at the Mn_3O_4 NPs−substrate interface, we proposed that the substrate-dependent OER activity of Mn_3O_4 NPs was mainly affected by the interfacial energy barrier and the consequent kinetics of the charge transport at the Mn_3O_4 NPs−substrate interface.

In our analysis, we assume that (i) our 4 nm-sized Mn_3O_4 nanocatalysts assembled on the substrate can be treated as a 150 nm-thick porous bulk film and (ii) the charge transfer between each nanoparticle is efficient. The charge transfer kinetics inside a thick film composed by Mn_3O_4 has been investigated quantitatively by using a new impedance model of our group.[30]

In addition, the Mn_3O_4 NPs−substrate interface could be influenced by the surface states of either catalysts or substrates. We conducted the same experiments with BF_4^- ligand-exchanged Mn_3O_4 NPs (Figure S3) and highly annealed substrates at 500 °C for 1 h (Figure S4).[45] The trend is consistent with that of Figure 2a. Furthermore, we compared the surface roughness by the electrochemical active surface area (ECSA) measurement (Figure S5) and observed that the double layer capacitances of Mn_3O_4 NPs were similar regardless of the underlying substrates (Figure S6). Therefore, in this experimental condition, the work function of the underlying substrate is a descriptor that explains the overall OER performance of Mn_3O_4 nanoparticles even after

controlling the surface states. It leads to the same conclusion. Therefore, it is valid to use the simplified interfacial band structure model to understand and explain the charge transport behaviors at the catalysts film—substrate interface.

We predicted that the OER performance could be controlled by tuning the interfacial Schottky barrier. Figure 4a illustrates the modulated interfacial band structure, in which an interlayer with a higher work function than the substrate, such as Au, Pt, and Ni, was inserted at the Mn_3O_4 NPs—substrate interface. The Fermi levels of the underlying substrate and the interlayer equilibrate with each other due to the metal—metal contact where the charge carriers freely transport. Thus, the interfacial energy barrier at the Mn_3O_4 NPs—interlayer interface was determined by the work function of the interlayer metal instead of that of the underlying substrate; therefore, facilitated interfacial charge transport and an enhanced OER performance were expected.

Figure 4b shows the interlayer-dependent OER performance of the Mn_3O_4 NPs/Ti electrode in neutral 0.5 M phosphate buffer solution. We introduced four different interlayers (Au,

Pt, Ni, and Cu with a thickness of 50 nm), for which the work functions were 5.10, 5.65, 5.15, and 4.65 eV, respectively.[44] As expected from the interfacial band structure, we observed an OER performance of Mn_3O_4 NPs that surpassed that of Mn_3O_4 NPs/Ti. While the catalytic performances for the cases using the Au, Pt, and Ni interlayers were recorded as similar to that of Mn_3O_4 NPs/FTO, the Mn_3O_4 NPs/Cu/Ti system exhibited a relatively poor OER performance, which corresponded to the observed tendency in Figure 2a. The fitting results of the EIS analysis for Mn_3O_4 NPs/Au/Ti and Mn_3O_4 NPs/Au/FTO, as shown in Figure 2c and d, clearly indicated a significant decrease in the total charge transfer resistance for the overall OER process (R1) by 8—30 times compared with the results for Mn_3O_4 NPs/Ti (Table S2). These data apparently supported our prediction that the Au interlayer facilitated charge transport at the Mn_3O_4 NPs—interlayer interface.

Additionally, to exclude a possible catalytic effect of the interlayer material, we varied the thickness of the Au interlayer and checked the OER performance with the Mn_3O_4 NPs/Au/Ti electrode (Figure 4c). Regardless of the interlayer thickness, the catalytic activities were identically monitored and exhibited similar overpotentials, indicating that the interlayer-dependent OER performance was independent of the catalytic activity of the interlayer. Therefore, we suggest that a metal interlayer deposition of only 10 nm thickness can sufficiently control the interfacial energy barrier at the Mn_3O_4 NPs—substrate interface. We expect that the insertion of thin interlayers with proper work functions can be a promising methodology for improving the poor OER performance accompanying the industrially relevant Ti substrate.

4. CONCLUSIONS

We demonstrated the importance of interfacial band structure between Mn_3O_4 NPs and the substrate for electrochemical water oxidation, which has not been considered in electro-catalytic systems. We observed that the work function of the underlying substrate affected the overall OER performance. Specifically, we observed that (i) the OER activity became poor as the work function of the substrate decreased and (ii) the OER activity became saturated as the work function of the substrate increased above a certain value. Those two phenomena could be explained by the interfacial band structure model, where a Schottky barrier hindered the interfacial transport of the charge carriers for water oxidation. On the basis of our understanding of the interfacial band structure, we improved the OER activity of Mn_3O_4 NPs on a poorly performing substrate such as Ti by inserting a thin interlayer with a high work function. We believe that our experimental findings and the theoretical understandings of the substrate effect provide new insights into the charge transport behaviors of film-type electrocatalysts and establish a strategy for the activity maximization of industrially relevant substrates, such as Ti.
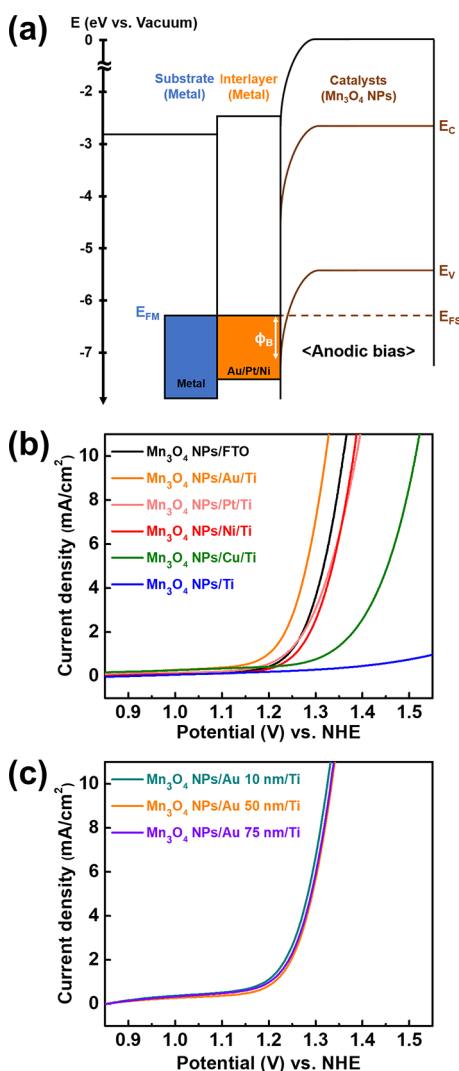

Figure 4. (a) Schematic band structure of the substrate—interlayer—catalysts interface. Polarization-corrected cyclic voltammetry curves of Mn_3O_4 nanoparticles for (b) different interlayers on Ti foil and (c) different Au thicknesses on Ti foil in 0.5 M phosphate buffer solution at pH 7 (scan rate: 50 mV/s).

■ ASSOCIATED CONTENT

Ⓢ Supporting Information

The Supporting Information is available free of charge at https://pubs.acs.org/doi/10.1021/acscatal.9b03831.

> XPS spectra of Mn_3O_4 NPs/FTO and Mn_3O_4 NPs/Ti; stability data of Mn_3O_4 NPs/substrates; CVs of Mn_3O_4 NPs with BF_4^- ligands/substrates; CVs of Mn_3O_4 NPs/

annealed substrates; ECSA data of Mn_3O_4 NPs/ substrates; OER performance of Mn_3O_4 NPs comparison with reported catalysts; and fitting results of EIS analysis (PDF)

■ AUTHOR INFORMATION

Corresponding Author
*E-mail: nkitae@snu.ac.kr.

ORCID
Moo Young Lee: 0000-0002-6788-9508
Sunghak Park: 0000-0001-9394-4833
Tae-Woo Lee: 0000-0002-6449-6725
Ki Tae Nam: 0000-0001-6353-8877

Author Contributions
§M.Y.L. and H.H. contributed equally.

Notes
The authors declare no competing financial interest.

■ REFERENCES

(1) Dresselhaus, M. S.; Thomas, I. L. Alternative energy technologies. *Nature* **2001**, *414*, 332−337.

(2) Bockris, J. O.; Veziroglu, T. N. Estimates of the price of hydrogen as a medium for wind and solar sources. *Int. J. Hydrogen Energy* **2007**, *32*, 1605−1610.

(3) Seh, Z. W.; Kibsgaard, J.; Dickens, C. F.; Chorkendorff, I.; Nørskov, J. K.; Jaramillo, T. F. Combining theory and experiment in electrocatalysis: Insights into materials design. *Science* **2017**, *355*, eaad4998.

(4) Man, I. C.; Su, H.-Y.; Calle-Vallejo, F.; Hansen, H. A.; Martínez, J. I.; Inoglu, N. G.; Kitchin, J.; Jaramillo, T. F.; Nørskov, J. K.; Rossmeisl, J. Universality in Oxygen Evolution Electrocatalysis on Oxide Surfaces. *ChemCatChem* **2011**, *3*, 1159−1165.

(5) Dau, H.; Limberg, C.; Reier, T.; Risch, M.; Roggan, S.; Strasser, P. The Mechanism of Water Oxidation: From Electrolysis via Homogeneous to Biological Catalysis. *ChemCatChem* **2010**, *2*, 724−761.

(6) McCrory, C. C. L.; Jung, S.; Ferrer, I. M.; Chatman, S. M.; Peters, J. C.; Jaramillo, T. F. Benchmarking Hydrogen Evolving Reaction and Oxygen Evolving Reaction Electrocatalysts for Solar Water Splitting Devices. *J. Am. Chem. Soc.* **2015**, *137*, 4347−4357.

(7) González-Huerta, R. G.; Ramos-Sánchez, G.; Balbuena, P. B. Oxygen evolution in Co-doped RuO_2 and IrO_2: Experimental and theoretical insights to diminish electrolysis overpotential. *J. Power Sources* **2014**, *268*, 69−76.

(8) Kadakia, K.; Datta, M. K.; Jampani, P. H.; Park, S. K.; Kumta, P. N. Novel F-Doped IrO_2 oxygen evolution electrocatalyst for PEM based water electrolysis. *J. Power Sources* **2013**, *222*, 313−317.

(9) Marshall, A.; Børresen, B.; Hagen, G.; Sunde, S.; Tsypkin, M.; Tunold, R. Iridium oxide-based nanocrystalline particles as oxygen evolution electrocatalysts. *Russ. J. Electrochem.* **2006**, *42*, 1134−1140.

(10) Cheng, J.; Zhang, H.; Ma, H.; Zhong, H.; Zou, Y. Preparation of $Ir_{0.4}Ru_{0.6}Mo_xO_y$ for oxygen evolution by modified Adams' fusion method. *Int. J. Hydrogen Energy* **2009**, *34*, 6609−6613.

(11) McCrory, C. C. L.; Jung, S.; Peters, J. C.; Jaramillo, T. F. Benchmarking Heterogeneous Electrocatalysts for the Oxygen Evolution Reaction. *J. Am. Chem. Soc.* **2013**, *135*, 16977−16987.

(12) Burke, M. S.; Enman, L. J.; Batchellor, A. S.; Zou, S.; Boettcher, S. W. Oxygen Evolution Reaction Electrocatalysis on Transition Metal Oxides and (Oxy)hydroxides: Activity Trends and Design Principles. *Chem. Mater.* **2015**, *27*, 7549−7558.

(13) Roger, I.; Symes, M. D. Efficient Electrocatalytic Water Oxidation at Neutral and High pH by Adventitious Nickel at Nanomolar Concentrations. *J. Am. Chem. Soc.* **2015**, *137*, 13980−13988.

(14) Chowdhury, D. R.; Spiccia, L.; Amritphale, S. S.; Paul, A.; Singh, A. A robust iron oxyhydroxide water oxidation catalyst operating under near neutral and alkaline conditions. *J. Mater. Chem. A* **2016**, *4*, 3655−3660.

(15) Wang, P.; Wan, L.; Lin, Y.; Wang, B. NiFe Hydroxide Supported on Hierarchically Porous Nickel Mesh as a High-Performance Bifunctional Electrocatalyst for Water Splitting at Large Current Density. *ChemSusChem* **2019**, *12*, 4038−4045.

(16) Kanan, M. W.; Nocera, D. G. In Situ Formation of an Oxygen-Evolving Catalyst in Neutral Water Containing Phosphate and Co^{2+}. *Science* **2008**, *321*, 1072−1075.

(17) Askerka, M.; Brudvig, G. W.; Batista, V. S. The O_2-Evolving Complex of Photosystem II: Recent Insights from Quantum Mechanics/Molecular Mechanics (QM/MM), Extended X-ray Absorption Fine Structure (EXAFS), and Femtosecond X-ray Crystallography Data. *Acc. Chem. Res.* **2017**, *50*, 41−48.

(18) Umena, Y.; Kawakami, K.; Shen, J.-R.; Kamiya, N. Crystal structure of oxygen-evolving photosystem II at a resolution of 1.9 Å. *Nature* **2011**, *473*, 55−60.

(19) Galstyan, A.; Robertazzi, A.; Knapp, E. W. Oxygen-Evolving Mn Cluster in Photosystem II: The Protonation Pattern and Oxidation State in the High-Resolution Crystal Structure. *J. Am. Chem. Soc.* **2012**, *134*, 7442−7449.

(20) Suga, M.; Akita, F.; Hirata, K.; Ueno, G.; Murakami, H.; Nakajima, Y.; Shimizu, T.; Yamashita, K.; Yamamoto, M.; Ago, H.; Shen, J.-R. Native structure of photosystem II at 1.95 Å resolution viewed by femtosecond X-ray pulses. *Nature* **2015**, *517*, 99−103.

(21) Zhang, B.; Sun, L. Why nature chose the Mn_4CaO_5 cluster as water-splitting catalyst in photosystem II: a new hypothesis for the mechanism of O−O bond formation. *Dalton Trans.* **2018**, *47*, 14381−14387.

(22) Birkner, N.; Nayeri, S.; Pashaei, B.; Najafpour, M. M.; Casey, W. H.; Navrotsky, A. Energetic basis of catalytic activity of layered nanophase calcium manganese oxides for water oxidation. *Proc. Natl. Acad. Sci. U. S. A.* **2013**, *110*, 8801−8806.

(23) Indra, A.; Menezes, P. W.; Zaharieva, I.; Baktash, E.; Pfrommer, J.; Schwarze, M.; Dau, H.; Driess, M. Active Mixed-Valent MnO_x Water Oxidation Catalysts through Partial Oxidation (Corrosion) of Nanostructured MnO Particles. *Angew. Chem., Int. Ed.* **2013**, *52*, 13206−13210.

(24) Zaharieva, I.; Najafpour, M. M.; Wiechen, M.; Haumann, M.; Kurz, P.; Dau, H. Synthetic manganese−calcium oxides mimic the water-oxidizing complex of photosynthesis functionally and structurally. *Energy Environ. Sci.* **2011**, *4*, 2400−2408.

(25) Robinson, D. M.; Go, Y. B.; Mui, M.; Gardner, G.; Zhang, Z.; Mastrogiovanni, D.; Garfunkel, E.; Li, J.; Greenblatt, M.; Dismukes, G. C. Photochemical Water Oxidation by Crystalline Polymorphs of Manganese Oxides: Structural Requirements for Catalysis. *J. Am. Chem. Soc.* **2013**, *135*, 3494−3501.

(26) Takashima, T.; Hashimoto, K.; Nakamura, R. Inhibition of Charge Disproportionation of MnO_2 Electrocatalysts for Efficient Water Oxidation under Neutral Conditions. *J. Am. Chem. Soc.* **2012**, *134*, 18153–18156.

(27) Jin, K.; Park, J.; Lee, J.; Yang, K. D.; Pradhan, G. K.; Sim, U.; Jeong, D.; Jang, H. L.; Park, S.; Kim, D.; Sung, N.-E.; Kim, S. H.; Han, S.; Nam, K. T. Hydrated Manganese(II) Phosphate $(Mn_3(PO_4)_2 \cdot 3H_2O)$ as a Water Oxidation Catalyst. *J. Am. Chem. Soc.* **2014**, *136*, 7435–7443.

(28) Jin, K.; Chu, A.; Park, J.; Jeong, D.; Jerng, S. E.; Sim, U.; Jeong, H.-Y.; Lee, C. W.; Park, Y.-S.; Yang, K. D.; Pradhan, G. K.; Kim, D.; Sung, N.-E.; Kim, S. H.; Nam, K. T. Partially Oxidized Sub-10 nm MnO Nanocrystals with High Activity for Water Oxidation Catalysis. *Sci. Rep.* **2015**, *5*, 10279.

(29) Jin, K.; Seo, H.; Hayashi, T.; Balamurugan, M.; Jeong, D.; Go, Y. K.; Hong, J. S.; Cho, K. H.; Kakizaki, H.; Bonnet-Mercier, N.; Kim, M. G.; Kim, S. H.; Nakamura, R.; Nam, K. T. Mechanistic Investigation of Water Oxidation Catalyzed by Uniform, Assembled MnO Nanoparticles. *J. Am. Chem. Soc.* **2017**, *139*, 2277–2285.

(30) Seo, H.; Jin, K.; Park, S.; Cho, K. H.; Ha, H.; Lee, K.-G.; Lee, Y. H.; Nguyen, D. T.; Randriamahazaka, H.; Lee, J.-S.; Nam, K. T. Mechanistic Investigation with Kinetic Parameters on Water Oxidation Catalyzed by Manganese Oxide Nanoparticle Film. *ACS Sustainable Chem. Eng.* **2019**, *7*, 10595–10604.

(31) Bediako, D. K.; Costentin, C.; Jones, E. C.; Nocera, D. G.; Savéant, J.-M. Proton-Electron Transport and Transfer in Electrocatalytic Films. Application to a Cobalt-Based O_2-Evolution Catalyst. *J. Am. Chem. Soc.* **2013**, *135*, 10492–10502.

(32) Morales-Guio, C. G.; Liardet, L.; Hu, X. Oxidatively Electrodeposited Thin-Film Transition Metal (Oxy)hydroxides as Oxygen Evolution Catalysts. *J. Am. Chem. Soc.* **2016**, *138*, 8946–8957.

(33) Kwon, G.; Jang, H.; Lee, J.-S.; Mane, A.; Mandia, D. J.; Soltau, S. R.; Utschig, L. M.; Martinson, A. B. F.; Tiede, D. M.; Kim, H.; Kim, J. Resolution of Electronic and Structural Factors Underlying Oxygen-Evolving Performance in Amorphous Cobalt Oxide Catalysts. *J. Am. Chem. Soc.* **2018**, *140*, 10710–10720.

(34) Doyle, R. L.; Lyons, M. E. G. An electrochemical impedance study of the oxygen evolution reaction at hydrous iron oxide in base. *Phys. Chem. Chem. Phys.* **2013**, *15*, 5224–5237.

(35) Zhang, J.; Zhang, Q.; Feng, X. Support and Interface Effects in Water-Splitting Electrocatalysts. *Adv. Mater.* **2019**, *31*, 1808167.

(36) Chakthranont, P.; Kibsgaard, J.; Gallo, A.; Park, J.; Mitani, M.; Sokaras, D.; Kroll, T.; Sinclair, R.; Mogensen, M. B.; Jaramillo, T. F. Effects of Gold Substrates on the Intrinsic and Extrinsic Activity of High-Loading Nickel-Based Oxyhydroxide Oxygen Evolution Catalysts. *ACS Catal.* **2017**, *7*, 5399–5409.

(37) Yeo, B. S.; Bell, A. T. Enhanced Activity of Gold-Supported Cobalt Oxide for the Electrochemical Evolution of Oxygen. *J. Am. Chem. Soc.* **2011**, *133*, 5587–5593.

(38) Jia, Q. X.; Wu, X. D.; Foltyn, S. R.; Findikoglu, A. T.; Tiwari, P.; Zheng, J. P.; Jow, T. R. Heteroepitaxial growth of highly conductive metal oxide RuO_2 thin films by pulsed laser deposition. *Appl. Phys. Lett.* **1995**, *67*, 1677–1679.

(39) El Khakani, M. A.; Chaker, M.; Gat, E. Pulsed laser deposition of highly conductive iridium oxide thin films. *Appl. Phys. Lett.* **1996**, *69*, 2027–2029.

(40) Jung, S.-K.; Kim, H.; Cho, M. G.; Cho, S.-P.; Lee, B.; Kim, H.; Park, Y.-U.; Hong, J.; Park, K.-Y.; Yoon, G.; Seong, W. M.; Cho, Y.; Oh, M. H.; Kim, H.; Gwon, H.; Hwang, I.; Hyeon, T.; Yoon, W.-S.; Kang, K. Lithium-free transition metal monoxides for positive electrodes in lithium-ion batteries. *Nat. Energy* **2017**, *2*, 16208.

(41) Lee, Y. H.; Park, S.; Lee, K.-G.; Lee, M. Y.; Cho, K. H.; Kim, S. J.; Nam, K. T. Methylamine Treated Mn_3O_4 Nanoparticles as a Highly Efficient Water Oxidation Catalyst under Neutral Condition. *ChemCatChem* **2019**, *11*, 1665–1672.

(42) Chun, W.-J.; Ishikawa, A.; Fujisawa, H.; Takata, T.; Kondo, J. N.; Hara, M.; Kawai, M.; Matsumoto, Y.; Domen, K. Conduction and Valence Band Positions of Ta_2O_5, TaON, and Ta_3N_5 by UPS and Electrochemical Methods. *J. Phys. Chem. B* **2003**, *107*, 1798–1803.

(43) Cahen, D.; Kahn, A. Electron Energetics at Surfaces and Interfaces: Concepts and Experiments. *Adv. Mater.* **2003**, *15*, 271–277.

(44) Michaelson, H. B. The work function of the elements and its periodicity. *J. Appl. Phys.* **1977**, *48*, 4729–4733.

(45) Dong, A.; Ye, X.; Chen, J.; Kang, Y.; Gordon, T.; Kikkawa, J. M.; Murray, C. B. A Generalized Ligand-Exchange Strategy Enabling Sequential Surface Functionalization of Colloidal Nanocrystals. *J. Am. Chem. Soc.* **2011**, *133*, 998–1006.